

High-resolution electrical detection of free induction decay and Hahn echoes in phosphorus-doped silicon

Jinming Lu,^{*} Felix Hoehne,[†] Andre R. Stegner, Lukas Dreher, Martin Stutzmann, and Martin S. Brandt
Walter Schottky Institut, Technische Universität München, Am Coulombwall 4, D-85748 Garching, Germany

Hans Huebl

Walther-Meißner-Institut, Bayerische Akademie der Wissenschaften, Walther-Meißner-Straße 8, 85748 Garching, Germany

(Received 28 January 2011; revised manuscript received 8 April 2011; published 1 June 2011)

Paramagnetic centers in a solid-state environment usually give rise to inhomogeneously broadened electron paramagnetic resonance (EPR) lines, making conventionally detected free induction decay (FID) signals disappear within the spectrometer dead time. Here, high-resolution experimental results of an electrically detected FID of phosphorus donors in silicon epilayers with natural isotope composition are presented, showing Ramsey fringes within the first 150 ns. An analytical model is developed to account for the data obtained as well as for the results of analogous two-pulse echo experiments. The results of a numerical calculation are further presented to assess the capability of the method to study the exchange interaction between the donor spins and paramagnetic interface defect states. In the current samples, an upper limit of 5 MHz is obtained for the average exchange interaction.

DOI: [10.1103/PhysRevB.83.235201](https://doi.org/10.1103/PhysRevB.83.235201)

PACS number(s): 71.55.Cn, 76.30.-v, 03.67.Lx, 73.50.Gr

I. INTRODUCTION

Solid-state based quantum computer (QC) architectures have recently attracted considerable interest due to the prospect of possible scalability. Several implementations have been proposed, such as superconducting tunnel junctions,¹ nuclear spins in crystal lattices,² electron spins localized in quantum dots (QDs),^{3,4} and nuclear⁵ or electron spins⁶ at donors.

Qubits based on phosphorus donor (³¹P) electron spins in silicon are promising candidates due to their long coherence times.⁷ For their manipulation, electron spin resonance experiments are usually employed. In the last few years, several concepts for the readout have been proposed. Single-shot electron spin readout has been demonstrated using a single-electron transistor coupled to implanted phosphorus donors.⁸ As alternatives, different methods based on electrically detected magnetic resonance (EDMR) have been proposed. These include spin-dependent scattering (SDS)^{9,10} of electrons in a two-dimensional electron gas, spin-dependent trapping,¹¹ or spin-dependent recombination (SDR) via spin pairs formed by ³¹P and paramagnetic Si/SiO₂ interface states.¹²⁻¹⁴

The sensitivity of SDR-based EDMR has been demonstrated by detecting the EDMR signal from less than 100 donors,¹⁵ providing the potential of reading out single donor qubits. The development of pulsed EDMR (pEDMR)¹⁶⁻¹⁸ has paved the way for studying dynamical properties of spin systems, such as coherence times T_2 ¹⁹ or spin-lattice relaxation times T_1 ²⁰ of phosphorus donors (³¹P) in silicon. While in SDS-based EDMR, a theoretical study proposed an optimal design concerning the depth of the implanted donor, which maximizes the amplitude of the detected signal,²¹ the existence of an optimal distance between the spin pair partners in SDR-based EDMR is still an open question.

Due to the overlap of the electron wave functions of the donor and the interface state, the exchange interaction (J coupling) is strongly dependent on the distance between the two spins.²² Since this interaction influences both the

energy eigenstates and the recombination rate of the spin pair,²³ its exact magnitude for a given intrapair distance is an important information for the optimal design of a potential QC using SDR-based EDMR as readout principle. An estimate of the exchange interaction within spin pairs in phosphorus doped silicon (Si:P) has been inferred from a theoretical model describing the experimentally determined magnetic field dependence of the continuous wave (cw) EDMR signal intensity.²⁴ However, this indirect approach only gives a rough estimate due to the uncertainty in the parameters involved.

In this paper, we present a detailed analysis of the time domain methods of electrically detected (ED) free induction decay (FID) and Hahn echo using a tomography technique developed earlier.¹⁹ It is shown that the EDFID technique could be used to measure the average exchange coupling between a ³¹P donor and a P_{b0} center at the Si/SiO₂ interface. Conventionally detected EPR-FID has not seen a widespread application for studies of paramagnetic species in solids since the broad Larmor frequency distribution usually encountered in solid-state spin systems makes the FID signal disappear on a time scale that is usually much shorter than the spectrometer dead time.²⁵⁻²⁷ Here, it is shown that by employing electrical detection, information within the dead time of conventional EPR-detected FID can be obtained.

In Secs. III A and III B high-resolution measurements on a ³¹P ensemble in silicon with natural isotope composition (^{nat}Si) are presented. It is shown that the EDFID signal is not disturbed during the spectrometer dead time. An analytical equation for negligible coupling is deduced to analyze the experimental data, demonstrating the agreement with the results obtained from the complementary frequency domain method of cwEDMR concerning the characterization of the Larmor frequency distribution. A numerical study in Sec. III C is performed to assess the EDFID technique in terms of its capability to quantitatively investigate the exchange coupling of spin pairs, providing an upper limit for the average exchange

coupling in ^{nat}Si and a possible way for a definite measurement using isotopically purified ^{28}Si .

II. EXPERIMENTAL DETAILS

The sample used in this work is fabricated by chemical vapor deposition and consists of a 22 nm thick ^{nat}Si layer with $[\text{P}] = 9 \times 10^{16} \text{ cm}^{-3}$ covered by a native oxide. It is grown on a 2.5 μm thick, nominally undoped ^{nat}Si buffer on a silicon-on-insulator substrate. Evaporated interdigit Cr/Au contacts with a period of 20 μm covering an active area of $2 \times 2.25 \text{ mm}^2$ are biased with 100 mV, resulting in a current of $\approx 80 \mu\text{A}$ under illumination with white light. The major paramagnetic states are identified in cwEDMR experiments performed in a Bruker X-band dielectric microwave resonator for pulsed EPR. The microwave frequency of $\nu_{\text{mw}} = \omega_{\text{mw}}/(2\pi) = 9.7400 \text{ GHz}$ is provided by an HP83640 microwave synthesizer. The measurements are performed at 5.5 K in a helium continuous flow cryostat. The samples are oriented in an external magnetic field B_0 with the [001] axis of the Si wafer parallel to B_0 .

The first derivative of the relative current change $\Delta I/I$ (see Fig. 1) is measured with magnetic field modulation and lock-in detection as a function of B_0 provided by a Bruker BE 25 electromagnet. We used the two pronounced ^{31}P hyperfine resonance lines [denoted hf(^{31}P)] at $B_0 = 346.17 \text{ mT}$ and $B_0 = 350.27 \text{ mT}$ to calibrate the magnetic field B_0 such that their center field corresponds to $g = 1.9985$.²⁸ In addition, a resonance line at $g = 2.0069 \pm 0.0004$ arising from the P_{b0} center at the Si/SiO₂ interface can be observed in accordance with previous studies for $B_0 \parallel [001]$.²⁹ A further resonance line is observed at $g = 2.0036 \pm 0.0004$ which, due to its g factor, is attributed to the P_{b1} center.³⁰ We are aware of the fact that there is no consensus in the literature on whether the P_{b1} defect is electrically active,^{31,32} and therefore measurements of the angular dependence of the g factor or the hyperfine interactions with ^{29}Si nuclei would be needed for an unambiguous identification. The small resonance line at $B_0 = 348.12 \text{ mT}$ could be attributed to conduction band electrons (CE) with a g factor of $g \approx 1.9990 \pm 0.0004$.³³ A fit assuming Gaussian line shapes and equal amplitudes of both ^{31}P resonance lines is indicated by the red line in Fig. 1. The decomposition of the fitted spectrum is shown in the lower part of Fig. 1. An analysis of the isolated high-field hf(^{31}P) line yields a peak-to-peak line width of $\Delta B_{\text{pp}}^{\text{cwEDMR}} = 0.30 \pm 0.03 \text{ mT}$ after correcting for the influence of magnetic field modulation.³⁴ This line broadening is predominantly inhomogeneous, caused by randomly oriented nuclear spins of the ^{29}Si isotope in natural Si, which give rise to an unresolved superhyperfine multiplet.³⁵ Homogeneous broadening only plays a minor role since T_1 and T_2 times of the ^{31}P donor spins determined by ED inversion recovery²⁰ and ED Hahn echo¹⁹ experiments on this sample yield $T_1 \approx 5.3 \mu\text{s}$ and $T_2 \approx 3.3 \mu\text{s}$, respectively, when the measured decays are fitted by a single exponential dependence.

The pulsed EDMR experiments are performed at a microwave frequency of $\nu_{\text{mw}} = \omega_{\text{mw}}/(2\pi) = 9.7331 \text{ GHz}$ under the same orientation of the sample as the cwEDMR experiments. For all pulsed measurements, the magnetic field B_0 is corrected by the magnetic field offset determined

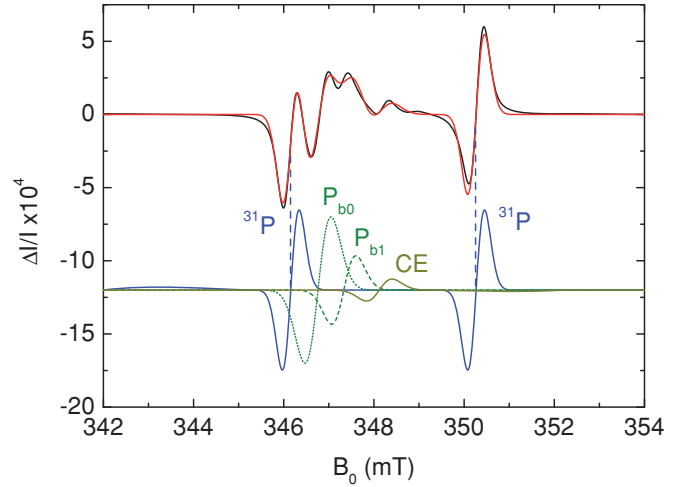


FIG. 1. (Color online) First derivative spectrum of the relative change $\Delta I/I$ of the photocurrent in a cwEDMR experiment on $^{nat}\text{Si:P}$ with a magnetic field modulation amplitude of 0.2 mT. The red curve represents a fit using Gaussian line shapes and equal amplitudes of both ^{31}P resonance lines. The constituent lines of the fit are shown below for better visibility.

by cwEDMR. The microwave pulses are shaped using a SPINCORE PulseBlasterESR-Pro 400 MHz pulse generator and a system of microwave mixers, and are then amplified by an Applied Systems Engineering 117X traveling wave tube with a maximum peak power of 1 kW. The actual pulse shapes coupled into the resonator are checked in reflection experiments. The quality factor of the dielectric resonator is adjusted to make a compromise between sufficient excitation bandwidth and a microwave magnetic field B_1 high enough for coherent spin manipulation. The adjustment of the microwave power is achieved by a tuneable attenuator; the $\pi/2$ -pulse time of $\tau_{\pi/2} = 15 \text{ ns}$ corresponding to $B_1 = 0.6 \text{ mT}$ used throughout this paper is determined in Rabi-oscillation experiments as previously developed.^{17,18} The current transients are acquired using a current amplifier followed by a voltage amplifier and a fast data acquisition card. To improve the signal-to-noise ratio, we applied a two-step phase cycling sequence where the phase of the last $\pi/2$ pulse was switched by 180° at a frequency of $\approx 5 \text{ Hz}$ and the signals for each phase are then subtracted from each other. Switching the phases at a frequency of several Hz has the same purpose as a lock-in detection scheme and improves the signal-to-noise ratio by reducing the effects of $1/f$ noise in the measurement setup.

III. RESULTS AND DISCUSSION

A. Electrically detected FID

The EDFID tomography is performed by a $\pi/2$ - τ - $\pi/2$ pulse sequence with varying evolution time τ , consisting of the conventional free induction pulse sequence $\pi/2$ - τ followed by a $\pi/2$ -projection pulse as usually applied in multipulse EDMR experiments.^{19,20} Hence, it coincides with the pulse sequence of the Ramsey experiment.³⁶ The photocurrent transients measured for each B_0 and τ are integrated over a fixed recording time interval satisfying the criteria described in Ref. 23, resulting in a charge difference ΔQ . Figure 2 shows

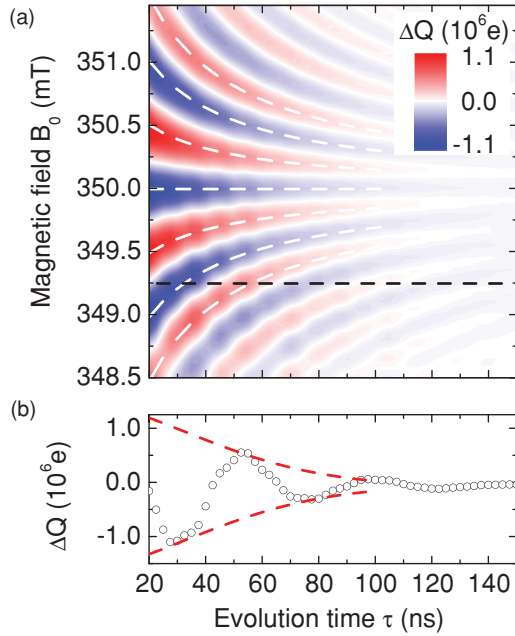


FIG. 2. (Color online) Electrically detected free induction decay or Ramsey experiment on the high-field hf(^{31}P) resonance. (a) Contour plot of ΔQ as a function of the external magnetic field B_0 and the free evolution time τ . White dashed curves mark the positions of local extrema of ΔQ described by Eq. (2). The black dashed line indicates the position where the cross-sectional chart shown in panel (b) is taken. (b) Cross section of ΔQ along the evolution time axis at $B_0 = 349.25$ mT. Red dashed curves illustrate the Gaussian-shape damping of the oscillation amplitude.

experimental results of an EDFID tomography experiment on the isolated high-field hf(^{31}P) line.

We will now show that the pattern in Fig. 2(a), which is characteristic of an EDFID, can be understood by a simple model in which the contribution of the state of each spin pair at the end of the second $\pi/2$ pulse is proportional to its projection onto the singlet state $|S\rangle$.^{17,18} Hence, the measured charge $Q \propto -S^{\text{av}}(\tau) = -\text{Tr}(|S\rangle\langle S|\hat{\rho})$ reveals the average singlet content of the spin pair ensemble described by the density operator $\hat{\rho}$. This is in contrast to conventional ESR, where for an FID the magnetization after a $\pi/2$ pulse is detected. For microwave frequencies close to the Larmor frequency of the high-field hf(^{31}P), the singlet content $S(\tau)$ of each spin pair reflects the dynamics of only this spin species¹⁷ while in a first approximation the spin state of P_{b0} is unaltered and just serves as a projection partner. This is justified since the separation of the Larmor frequencies of the ^{31}P and P_{b0} spins for the high-field hf(^{31}P) resonance is approximately one order of magnitude larger than the on-resonance Rabi frequency $\omega_1 = g\mu_B B_1/\hbar$. The minor effects of the off-resonance excitation of the other resonance lines can be seen as small oscillations on the Ramsey pattern in Fig. 2(a) at magnetic fields lower than 350 mT. We also neglect spin-spin interaction and incoherent processes during the pulse sequence. The former will be addressed in Sec. III C and the latter is a valid assumption since the time constant for the fastest incoherent process is $T_2 \approx 3.3 \mu\text{s}$ as measured in ED Hahn echo decay experiments on this sample. With

these assumptions, an expression for the theoretically expected signal

$$\Delta Q \propto -\exp\left[-\frac{1}{2}\frac{\sigma_\omega^2\tilde{\omega}_1^2}{\sigma_\omega^2 + \tilde{\omega}_1^2}\tau^2\right]\cos\left[\frac{\tilde{\omega}_1^2}{\sigma_\omega^2 + \tilde{\omega}_1^2}\Delta\omega\tau\right] \quad (1)$$

with $\tilde{\omega}_1 = \omega_1/\sqrt{2}$ and $\Delta\omega = \omega_0 - \omega_{\text{mw}}$ can be derived following Refs. 37,38 as shown in the Appendix. In Eq. (1), σ_ω quantifies the width of the Larmor frequency distribution as defined in Eq. (A5). The locations of the local extrema of ΔQ are given by Eq. (A8) as

$$B_0 - B_{\text{res}} = \frac{n\pi\hbar[1 + 2(\sigma_\omega/\omega_1)^2]}{g\mu_B} \frac{1}{\tau}, \quad n \in \mathbb{Z}, \quad (2)$$

representing hyperbolas in the B_0 - τ plane. These hyperbolas fit the experimentally observed pattern well, as evident from the white dashed curves in Fig. 2(a). The exponential term in Eq. (1) describes an envelope in the time domain which shows an $\exp[-(\tau/T_{\text{FID}})^2]$ -type decay behavior³⁹ as depicted by red dashed line in Fig. 2(b) with the time constant

$$T_{\text{FID}} = \sqrt{\frac{2}{\sigma_\omega^2} + \frac{4}{\omega_1^2}}. \quad (3)$$

This implies that for short pulses, i.e., in the high microwave power limit, T_{FID} is inversely proportional to the width of the Larmor frequency distribution and thus $\Delta B_{\text{pp}}^{\text{cwEDMR}}$ of the hf(^{31}P) resonance line in cwEDMR. The actual decay characteristics deviate from the $\exp[-(\tau/T_{\text{FID}})^2]$ behavior since the line shape is a convolution of a Gaussian and Lorentzian line shape rather than a pure Gaussian.

In Fig. 3(a), cross sections of ΔQ along the evolution time axis taken at different values of B_0 are plotted as a function of the evolution time τ , revealing strongly damped oscillations. These characteristics are consistent with those described by Eq. (1). A clear dependence of the frequencies of the damped oscillations ν_{FID} on the external magnetic field B_0 can be observed. The red lines in Fig. 3(a) show fits of the oscillations by the function

$$\Delta Q \sim -Ae^{-\left(\frac{\tau+\tau_0}{T_{\text{FID}}}\right)^2}\cos[2\pi\nu_{\text{FID}}(\tau + \tau_0)], \quad (4)$$

which is based on the model given in Eq. (1). In all the fits shown in Fig. 3(a), a global phase correction of $\tau_0 \approx 20$ ns has to be taken into account which is comparable to the overall pulse length of 30 ns. It can be attributed to the fact that dephasing during the pulse times cannot be neglected due to the finite pulse width compared to the evolution time τ . The values of ν_{FID} obtained from the fits are plotted as a function of the external magnetic field B_0 and displayed in Fig. 3(b). A clear linear dependence of ν_{FID} on the magnetic field B_0 can be observed as expected from Eq. (1),

$$\nu_{\text{FID}} = \frac{1}{2\pi} \frac{\tilde{\omega}_1^2}{\sigma_\omega^2 + \tilde{\omega}_1^2} (\omega_0 - \omega_{\text{mw}}) = k(B_0 - B_{\text{res}}), \quad (5)$$

with $k = g\mu_B/[h(1 + 2(\sigma_\omega/\omega_1)^2)]$. This is consistent with the linear dependence of the oscillation frequency on the detuning in a Ramsey experiment.^{40,41} From a linear fit of the data the value of $B_{\text{res}} = 350.02 \pm 0.01$ mT is obtained, which corresponds to the center position of the high-field hf(^{31}P) resonance line. Using Eq. (3) and $2\pi/\omega_1 = 60$ ns, the average

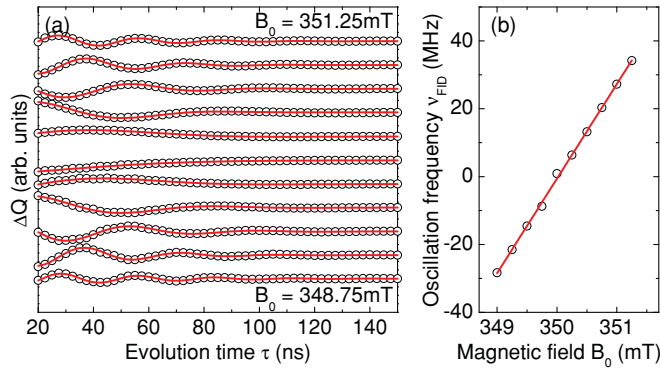


FIG. 3. (Color online) Oscillations in the evolution time domain. (a) Cross sections of ΔQ along the evolution time axis taken at different values of B_0 . The damping of the oscillations indicates that the spin ensemble dephases. Red curves are fits based on the model given by Eq. (4). (b) Frequency ν_{FID} of the damped oscillations as a function of the external magnetic field B_0 shows a linear behavior as expected from Eq. (5).

value $T_{\text{FID}} = 64.4 \pm 5$ ns obtained from the fits of the damped oscillations can be related to an expected cwEDMR peak-to-peak line width of $\Delta B_{\text{pp}}^{\text{FID}} = 2\hbar\sigma_\omega/(g\mu_B) = 0.26 \pm 0.02$ mT. This is in agreement with the result obtained from cwEDMR $\Delta B_{\text{pp}}^{\text{cwEDMR}} = 0.30 \pm 0.03$ mT, demonstrating the consistency of the experiments.

B. Electrically detected Hahn echo

Electrically detected echo sequences have been previously used to study T_2 ¹⁹ and T_1 times²⁰ of phosphorus donors near Si/SiO₂ interface defects. In this section, we will present detailed experimental results of the electrically detected Hahn echo measurement with a focus on the fine structure of the echo response.

The echo is measured using the previously developed tomography technique¹⁹ extending the pulse sequence $\pi/2$ - τ_1 - π - τ_2 of the conventional two-pulse spin echo containing two free evolution times τ_1 and τ_2 by a final $\pi/2$ pulse as applied in the EDFID technique. The measurements are conducted under the same experimental conditions as the EDFID experiments.

Figure 4 shows experimental results of an ED spin echo tomography experiment on the isolated high-field hf(³¹P) line with $\tau_1 = 300$ ns held fixed. The values of ΔQ plotted as a function of B_0 and τ_2 [Fig. 4(a)] are obtained in the same way as described in the EDFID section. Cross sections along the evolution time axis are displayed in Fig. 4(b). The red curve taken at the resonance field $B_0 = 350.0$ mT shows a Gaussian-shaped peak centered around $\tau_2 = \tau_1 = 300$ ns. The cross section of ΔQ at the off-resonance field $B_0 = 350.5$ mT, which is represented by the blue curve, shows oscillations as a function of the evolution time τ_2 with a maximum at $\tau_2 = \tau_1 = 300$ ns, which decay for $|\tau_2 - \tau_1| \gg 100$ ns.

The characteristic pattern indicated by the black dashed hyperbolas can be understood by the same quantitative model described in the previous section on EDFID. The singlet content $S(\tau)$ proportional to the recombination probability $P_{\uparrow,\downarrow}$ of a single spin after a $\pi/2$ - τ_1 - π - τ_2 - $\pi/2$ pulse sequence can be calculated using the matrix formalism described in

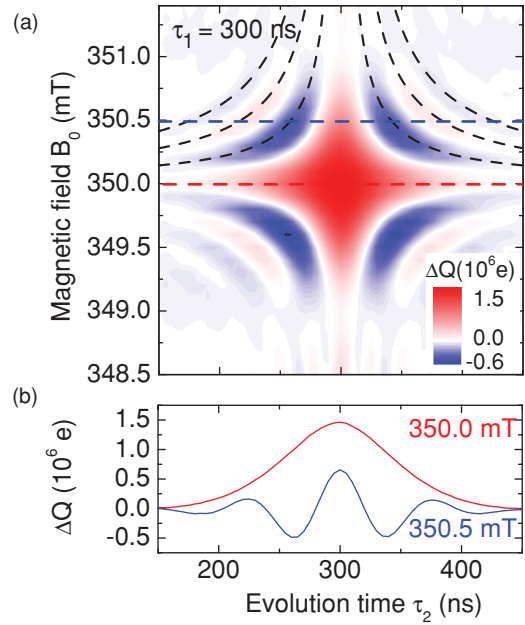


FIG. 4. (Color online) Electrically detected two-pulse Hahn echo on the high-field hf(³¹P) resonance with $\tau_1 = 300$ ns. (a) Contour plot of ΔQ as a function of the external magnetic field B_0 and the free evolution time τ_2 . Black dashed lines mark the hyperbola pattern according to Eq. (6). Red and blue dashed lines indicate positions where cross-sectional diagrams shown in panel (b) are taken. (b) Cross section of ΔQ along the evolution time axis at resonance condition (red line, $B_0 = 350.0$ mT) and for the off-resonant case (blue line, $B_0 = 350.5$ mT). Please refer to the text for details.

Refs. 37,38. For a Larmor frequency distribution modeled by a Gaussian with standard deviation σ_ω centered about ω_0 , we can derive analogously to Eq. (A7) that

$$\Delta Q \propto \exp\left[-\frac{1}{2} \frac{\sigma_\omega^2 \bar{\omega}_1^2}{\sigma_\omega^2 + \bar{\omega}_1^2} (\tau_2 - \tau_1)^2\right] \times \cos\left[\frac{\bar{\omega}_1^2}{\sigma_\omega^2 + \bar{\omega}_1^2} (\omega_0 - \omega_{\text{mw}})(\tau_2 - \tau_1)\right] \quad (6)$$

with $\bar{\omega}_1 = \omega_1/2$ ⁴².

Similar to the analysis of the EDFID experiment, various cross sections of ΔQ along the evolution time axis are taken and shown in Fig. 5(a). Data fitting based on Eq. (6) is performed and illustrated by the red curves. The oscillation frequency ν_{echo} obtained from the fits is plotted as a function of the external magnetic field B_0 [Fig. 5(b)], where a linear dependence of ν_{echo} as a function of B_0 can be observed as expected from

$$\nu_{\text{echo}} = \frac{1}{2\pi} \frac{\bar{\omega}_1^2}{\sigma_\omega^2 + \bar{\omega}_1^2} (\omega_0 - \omega_{\text{mw}}) = k'(B_0 - B_{\text{res}}), \quad (7)$$

with $k' = g\mu_B/[h(1 + 4(\sigma_\omega/\omega_1)^2)]$ analogous to Eq. (5). The exponential term in Eq. (6) describes a Gaussian envelope in the time domain with full width at half maximum (FWHM)

$$W_{\text{echo}} = 2\sqrt{2 \ln 2} \sqrt{\frac{1}{\sigma_\omega^2} + \frac{4}{\omega_1^2}}. \quad (8)$$

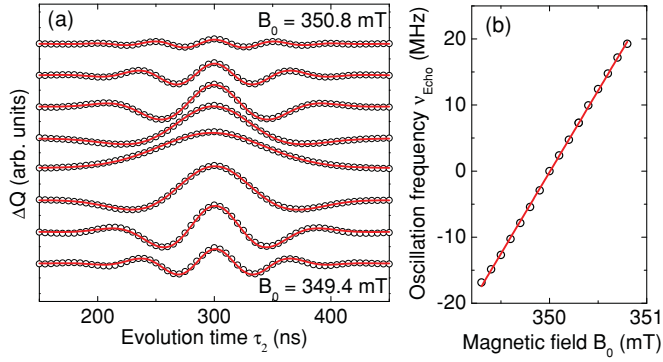


FIG. 5. (Color online) Oscillations in the evolution time domain. (a) Cross sections of ΔQ along the evolution time axis taken at different values of B_0 . Red curves are fits based on the model given by Eq. (6). (b) The frequency ν_{Echo} of the damped oscillations as a function of the external magnetic field B_0 shows a linear behavior as expected from Eq. (7).

From the fits of the data, an average value of $W_{\text{Echo}} = 106.9 \pm 4$ ns is obtained, corresponding to an expected cwEDMR linewidth of $\Delta B_{\text{pp}}^{\text{Echo}} = 0.28 \pm 0.01$ mT. This value is consistent with the values $\Delta B_{\text{pp}}^{\text{cwEDMR}} = 0.30 \pm 0.03$ mT and $\Delta B_{\text{pp}}^{\text{FID}} = 0.26 \pm 0.02$ mT obtained from previous experiments within the accuracy limits. Therefore, the ED Hahn echo response on the high-field $hf(^{31}\text{P})$ resonance shows the same fine structure as the EDFID experiment and can be explained by the same model as expected from the fact that the echo pulse sequence consists of two FIDs back to back.⁴³ However, the small oscillations seen in EDFID are not observed in the ED Hahn echo response, since they are not refocused by the additional central π pulse.

C. Spin-spin coupling

So far the experimental results have been discussed in the context of off-resonance oscillations and dephasing due to inhomogeneous line broadening. In different previous studies,^{23,24} the possible impact of coupling between the partners of the spin pair on EDMR experiments has been discussed. In the following, results of a numerical study of the EDFID experiment discussed above are presented, focusing on the possibility of EDFID to estimate the coupling strength.

The system is modeled by an ensemble of spin $S = 1/2$ pairs described by the density operator $\hat{\rho}$. The Hamiltonian of an individual pair is defined as

$$\hat{\mathcal{H}} = \hat{\mathcal{H}}_0 + \hat{\mathcal{H}}_J + \hat{\mathcal{H}}_1(t) \quad (9)$$

with

$$\begin{aligned} \hat{\mathcal{H}}_0 = & \frac{1}{2} g_P \mu_B (B_0 \pm B_{\text{HF}}/2 + B_{\text{SHF}}) \hat{\sigma}_z^{\text{P}} \\ & + \frac{1}{2} g_{\text{db}} \mu_B (B_0 + B_{\Delta\text{db}}) \hat{\sigma}_z^{\text{db}} \end{aligned} \quad (10)$$

representing the static uncoupled Hamiltonian in the presence of a constant magnetic field $\mathbf{B}_0 = B_0 \mathbf{e}_z$ superimposed with the hyperfine field of ^{31}P $B_{\text{HF}} = 4.2$ mT and the superhyperfine field B_{SHF} at the position of the donor, where the latter can be considered fixed for time scales shorter than the precession period of the ^{29}Si nucleus.⁴⁴ $B_{\Delta\text{db}}$ is the local shift of the static magnetic field at the position of the P_{b_0} center due to

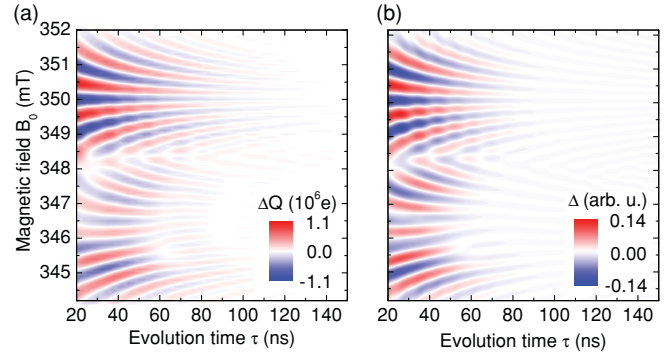


FIG. 6. (Color online) (a) Experimental results of the EDFID measurement showing all spectral features. (b) Simulation for $J = 0$ MHz. In both simulation and experimental results, the characteristic Ramsey pattern can be clearly seen at the position of the high-field $hf(^{31}\text{P})$ resonance, whereas the patterns at the low-field $hf(^{31}\text{P})$ and the P_{b_0} resonances are more complicated due to mutual interference.

effects such as disorder and superhyperfine interactions. The $\hat{\sigma}_{x,y,z}$ denote the Pauli spin operators. The circularly polarized microwave of angular frequency ω_{mw} and magnitude B_1 are represented in the rotating frame by

$$\hat{\mathcal{H}}_1 = \mu_B B_1 (g_P \hat{\sigma}_x^{\text{P}} + g_{\text{db}} \hat{\sigma}_x^{\text{db}}), \quad (11)$$

which is nonzero during the pulse. Spin-spin interaction is modeled by an exchange coupling Hamiltonian represented by

$$\hat{\mathcal{H}}_J = \hbar J \hat{\sigma}^{\text{P}} \cdot \hat{\sigma}^{\text{db}}/4, \quad (12)$$

with $\hat{\sigma} = (\hat{\sigma}_x, \hat{\sigma}_y, \hat{\sigma}_z)^T$. The dipolar coupling is smaller than 1 MHz for interspin distances larger than 3 nm, which is neglected here for simplicity. The simulation of the spin pair ensemble dynamics is based on the Liouville equation $\partial_t \hat{\rho} = i[\hat{\rho}, \hat{\mathcal{H}}]/\hbar$ in which, in contrast to Eq. (5) of Ref. 17, all terms related to incoherent processes are dropped since the time constant of the fastest incoherent process is more than one order of magnitude larger than the duration of the pulse sequence, as already mentioned in Sec. II. The initial steady state of the density operator is assumed to be given by the pure triplet state $\hat{\rho}^S = (|T_+\rangle\langle T_+| + |T_-\rangle\langle T_-|)/2$ with $|T_+\rangle = |\uparrow^{\text{db}}\uparrow^{\text{P}}\rangle$ and $|T_-\rangle = |\downarrow^{\text{db}}\downarrow^{\text{P}}\rangle$.¹⁷ For triplet recombination rates much smaller than the singlet recombination rate, the observable $Q(\tau)$ reflecting the state of the pair ensemble at the end of the second $\pi/2$ pulse assumes the form $Q(\tau) \propto -\delta(\tau) = -(\delta\rho_{\uparrow^{\text{db}}\downarrow^{\text{P}}} + \delta\rho_{\downarrow^{\text{db}}\uparrow^{\text{P}}})$,²³ where $-\delta\rho_{ii} = -[\rho_{ii}(\tau) - \rho_{ii}^S]$ denotes the negative difference between the diagonal elements of the density matrix at the end of the second $\pi/2$ pulse and the initial steady state. The negative sign expresses the quenching of the photocurrent due to recombination. Inhomogeneous line broadening is taken into account by calculating $-\delta(\tau)$ for a single spin pair and subsequent averaging over Gaussian distributions for both B_{SHF} and $B_{\Delta\text{db}}$ with experimentally obtained standard deviations from the pulsed EDFID spectrum shown in Fig. 6. Furthermore, the simulation takes all four combinations of spin pair formation into account, which arise from the two resonance positions of ^{31}P , the P_{b_0} , and the P_{b_1} .

Figure 6(a) shows the complete experimental results encompassing all resonances of the EDFID tomography experiment discussed in Fig. 2(a). Figure 6(b) shows the simulation of $-\delta$ for $J = 0$ as a function of B_0 and τ after subtraction of a constant background obtained from the value of $-\delta$ for large τ , resulting in the quantity Δ which can be compared to ΔQ in the experiment. The characteristic patterns of simulation and experiment fit quite well. At the high-field ^{31}P resonance, small oscillations superimposed on the Ramsey oscillation pattern can be seen in the experimental data as well as in the simulation. These small oscillations are due to the partial excitation of the low-field ^{31}P and the P_{b0} spins by the microwave pulses on the high-field ^{31}P resonance. Details of these patterns are shown in the Fourier transformed data in Figs. 7(a) and 7(b). The linear dependence of the oscillation frequency on $B_0 - B_{\text{res}}$ described by Eq. (5) is clearly visible in the frequency domain. The two ^{31}P resonances and the P_{b0} resonance are marked by black and white dashed lines, respectively. The P_{b1} resonance is not resolved due to the spectral overlap with the P_{b0} and its smaller amplitude. For better visibility, details of the FFT spectrum near the high-field $hf(^{31}\text{P})$ resonance are shown in panels (c) and (d) after subtracting a background of the form of Eq. (4) from the experimental and simulated data. Again, the low-field $hf(^{31}\text{P})$ resonance and the P_{b0} resonance are marked by black and white dashed lines. An additional resonance, indicated by the solid white line, can be seen in the experimental data. Its spectral position is in accordance with the small central line observed in cwEDMR (see Fig. 1). This line is not taken into account in the simulation. The intensity of the Fourier amplitude of the lines as a function of the magnetic field can be described by an equation of the form $\sin^2[\frac{\pi}{4}\sqrt{1+x^2}/(1+x^2)]$, analogous to Eq. (A1). In particular, the minima at frequencies of ≈ 65 MHz and ≈ 130 MHz correspond to rotations of the spins by integer multiples of 2π .

The simulation is further extended to nonzero coupling parameters with the focus on the clearly observable pattern structure on the high-field $hf(^{31}\text{P})$ resonance, which is shown in Fig. 8. Starting from $J = 0$, the exchange coupling parameter is increased in steps of 5 MHz resulting in a change of the qualitative behavior of the characteristic pattern. Whereas for $J = 0$ each hyperbola (cf. Fig. 2) either indicates positions of local maxima or minima, the values of Δ on each hyperbola oscillate as a function of τ for $J \neq 0$. This behavior can be clearly observed on the axis of symmetry at $B_0 = B_{\text{res}}$, which is displayed in Fig. 9(a) for different values of J .

For vanishing coupling, Δ relaxes exponentially to the equilibrium. For larger values of J , damped oscillations of Δ with frequency J are formed decaying to the equilibrium within the dephasing time T_{FID} . Compared with the existing experimental data [cf. Fig. 3(a)], the coupling is estimated $\ll 5$ MHz. Please note that in these simulations only the high-field ^{31}P and the P_{b0} are taken into account. Therefore, the small oscillations in Fig. 9 are due to off-resonance excitations of the P_{b0} spins.

Clearer insight might be obtained in experiments using isotopically purified ^{28}Si samples as shown in the simulation in Figs. 9(b)–9(d) where the line broadening is modeled by Lorentzian distributions with FWHM linewidths of 0.006 mT,

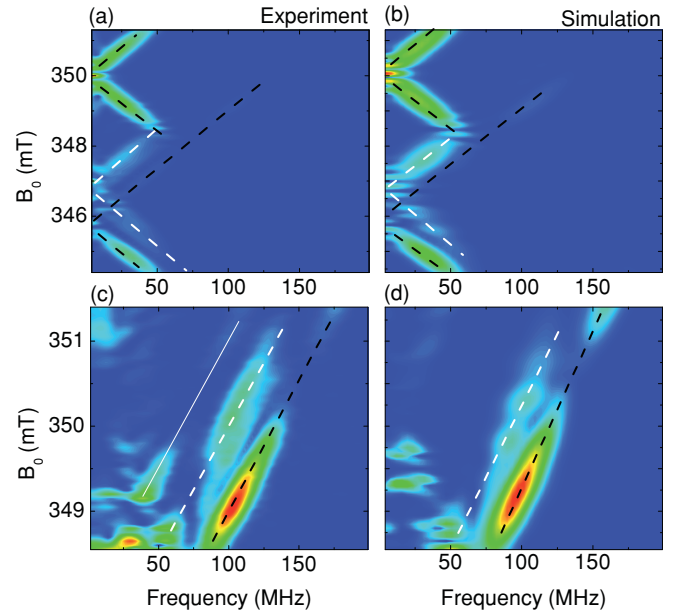


FIG. 7. (Color online) (a) and (b) Fourier transformation of the EDFID tomography experiment and simulation shown in Fig. 6. The linear dependence of the oscillation frequency on $B_0 - B_{\text{res}}$ described by Eq. (5) is clearly seen in the frequency domain. The two ^{31}P resonances and the broader P_{b0} resonance are marked by black and white dashed lines, respectively. (c) and (d) For better visibility, details of the FFT spectrum near the high-field $hf(^{31}\text{P})$ resonance are shown after subtracting a background of the form of Eq. (4) from the experimental and simulated data. Again, the low-field $hf(^{31}\text{P})$ resonance and the P_{b0} resonance are marked by black and white dashed lines. An additional resonance, indicated by the solid white line, can be seen in the experimental data. Its spectral position is in accordance with the small central line observed in cwEDMR (see Fig. 1).

0.023 mT, and 0.08 mT, respectively, corresponding to concentrations of ^{29}Si nuclei of 0.08%, 0.2%, and 1%, as indicated in the graphs.^{35,45} Since $T_{\text{FID}} \sim 1/\sigma_\omega$ [cf. Eq. (3)], oscillations on the axis of symmetry could be observed within the dephasing time also for weak J . Qualitatively, the frequency of the oscillations increases with increasing J as evident from Figs. 9(b)–9(d). Furthermore, it should be noted that only a moderate purification of Si (1% of ^{29}Si) is sufficient to improve the estimate for J . In the general case, distributions of exchange interaction as well as dipolar interaction have to be taken into account,¹⁷ which would result in an averaging out of the oscillation pattern. However, previous studies have revealed that only spin pairs within a narrow range of intrapair distances contribute to the observed signals,²⁰ which should make an estimate of J of contributing spin pairs still possible.

IV. SUMMARY

To summarize, we have used pulsed EDMR to study the free induction decay of phosphorus donor spins in silicon. We can resolve oscillations up to 150 ns limited by dephasing due to superhyperfine interactions with surrounding ^{29}Si nuclei. An analytical model is used to describe the FID of an inhomogeneously broadened line which is in good agreement with the experimental data. In addition, structures

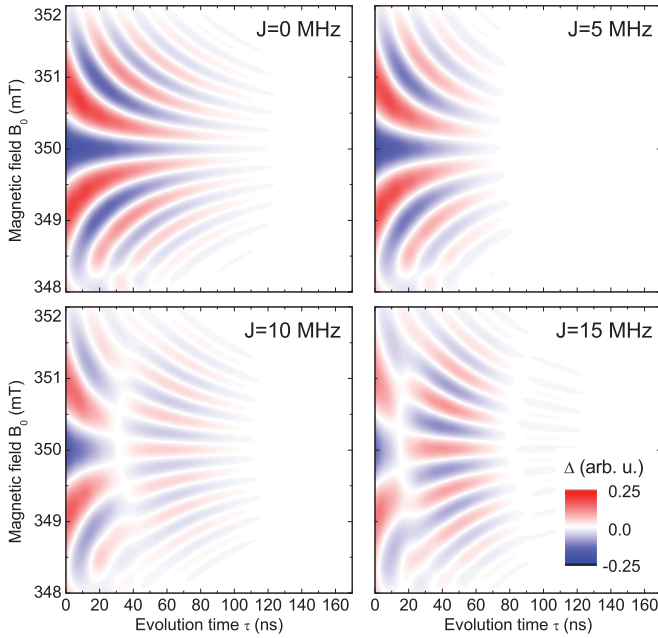


FIG. 8. (Color online) Simulation of the EDFID experiment at the high-field $hf(^{31}\text{P})$ resonance for different exchange coupling parameter. An oscillation of the signal in the time domain with the coupling frequency is expected. This oscillation is masked by the exponential decay of the signal due to dephasing and therefore can only be resolved for $J > 5$ MHz.

on two-pulse electron spin echoes have been measured which can be described by the same analytical model. The results of a numerical calculation are further presented and compared with the experimental data to assess the capability of the method to study spin-spin interactions. From these results, we can give an upper bound for the coupling parameter of $J \approx 5$ MHz in the samples studied.

ACKNOWLEDGMENTS

The work was financially supported by DFG (Grant No. SFB 631, C3) with additional support by the BMBF via EPR-Solar.

APPENDIX: ANALYTICAL EXPRESSION DESCRIBING THE EDFID PATTERN

In this section, Eq. (2) used to describe the pattern in Fig. 2(a) is derived. Neglecting spin-spin interactions and incoherent processes, the singlet content $S(\tau)$ is proportional to the flipping probability $P_{\uparrow,\downarrow}$ of a single spin after a $\pi/2$ - τ - $\pi/2$ pulse sequence, which has been investigated in studies related to nuclear magnetic resonance,^{37,38}

$$P_{\uparrow,\downarrow}(\tau) = 4 \sin^2 \theta \sin^2 \left(\frac{a\tau_p}{2} \right) \times \left[\cos \left(\frac{\lambda\tau}{2} \right) \cos \left(\frac{a\tau_p}{2} \right) - \cos \theta \sin \left(\frac{\lambda\tau}{2} \right) \sin \left(\frac{a\tau_p}{2} \right) \right]^2 \quad (\text{A1})$$

with

$$\lambda = \omega_S - \omega_{\text{mw}}, \quad a = \sqrt{\lambda^2 + \omega_1^2}, \quad \sin \theta = \frac{\omega_1}{a},$$

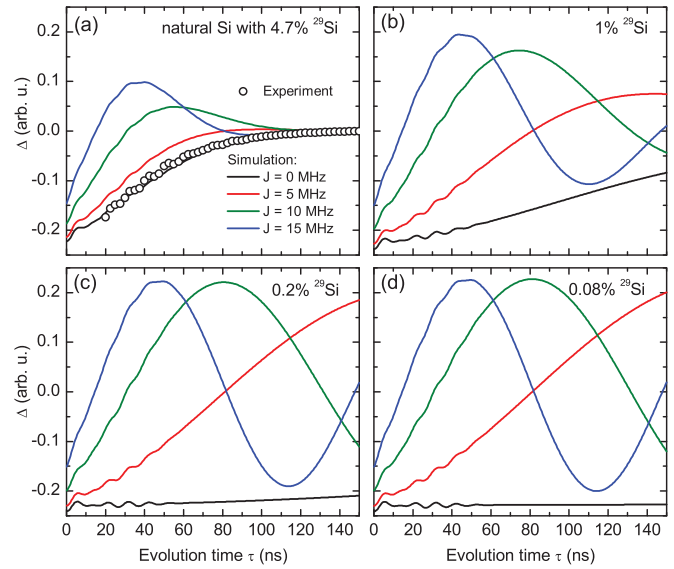


FIG. 9. (Color online) (a) Cross section along the τ axis at the high-field resonance field of ^{31}P of the experimental data (open circles) and the simulated data (solid lines) for different exchange coupling parameter between ^{31}P and P_{b0} . (b)–(d) Simulated data as in (a) for isotopically purified ^{28}Si samples with different concentrations of ^{29}Si . Here, more oscillations caused by the weak coupling can be seen due to the longer dephasing time.

where ω_S is the Larmor frequency of the ^{31}P donor electron and ω_{mw} the microwave frequency. $t_p = \pi/(2\omega_1)$ and τ denote the length of the $\pi/2$ pulse and the free evolution time, respectively. For inhomogeneously broadened lines, the observable $S^{\text{av}}(\tau)$ is obtained by averaging $S(\tau) \propto P_{\uparrow,\downarrow}(\tau)$ over the Larmor frequency distribution¹⁷

$$S^{\text{av}}(\tau) \propto \int_{-\infty}^{\infty} \Phi(\omega_S) P_{\uparrow,\downarrow}(\tau, \omega_S) d\omega_S. \quad (\text{A2})$$

For distributions $\Phi(\omega_S)$ with a maximum at the center frequency ω_0 , the dominant term of $S^{\text{av}}(\tau)$ for ω_{mw} close to ω_0 is given by

$$S^{\text{av}}(\tau) \propto \int_{-\infty}^{\infty} \Phi(\omega_S) \frac{\sin^2 \left(\frac{\pi}{2} \sqrt{1+x^2} \right)}{1+x^2} \frac{1 + \cos(\lambda\tau)}{2} d\omega_S, \quad (\text{A3})$$

with $x = \lambda/\omega_1$, neglecting a term of $O(|\omega_{\text{mw}} - \omega_S|^2)$. To obtain an analytical expression, Eq. (A3) can be further simplified by the approximation

$$\frac{\sin^2 \left(\frac{\pi}{2} \sqrt{1+x^2} \right)}{1+x^2} \approx \exp(-x^2) \quad (\text{A4})$$

since both functions share the same leading orders in the Taylor expansion, tolerating a deviation of 6% in the integrated area within the interval defined by the zero crossings of $\sin^2(\dots)/(1+x^2)$ in Eq. (A3). Modeling the Larmor frequency distribution by a Gaussian

$$\Phi(\omega_S) = \frac{1}{\sqrt{2\pi}\sigma_\omega} \exp \left[-\frac{1}{2} \left(\frac{\omega_S - \omega_0}{\sigma_\omega} \right)^2 \right] \quad (\text{A5})$$

with standard deviation σ_ω and center ω_0 , the average singlet content is given by

$$S^{\text{av}} \propto \exp\left[-\frac{1}{2}\frac{\Delta\omega^2}{\sigma_\omega^2 + \tilde{\omega}_1^2}\right] \left\{ 1 + \exp\left[-\frac{1}{2}\frac{\sigma_\omega^2 \tilde{\omega}_1^2}{\sigma_\omega^2 + \tilde{\omega}_1^2}\tau^2\right] \times \cos\left[\frac{\tilde{\omega}_1^2}{\sigma_\omega^2 + \tilde{\omega}_1^2}\Delta\omega\tau\right] \right\} \quad (\text{A6})$$

with $\tilde{\omega}_1 = \omega_1/\sqrt{2}$ and $\Delta\omega = \omega_0 - \omega_{\text{mw}}$. Since $Q \propto -S^{\text{av}}$, ΔQ is proportional to $-[S^{\text{av}}(\tau) - S^{\text{av}}(\tau \rightarrow \infty)]$ as the constant background given by $S^{\text{av}}(\tau \rightarrow \infty)$ is identical for the signals obtained for both phases ($+x$ and $-x$) of the last $\pi/2$

pulse and thus subtracted by the data evaluation procedure described in Sec. II. This results in

$$\Delta Q \propto -\exp\left[-\frac{1}{2}\frac{\sigma_\omega^2 \tilde{\omega}_1^2}{\sigma_\omega^2 + \tilde{\omega}_1^2}\tau^2\right] \cos\left[\frac{\tilde{\omega}_1^2}{\sigma_\omega^2 + \tilde{\omega}_1^2}\Delta\omega\tau\right] \quad (\text{A7})$$

with local extrema approximately determined by values of B_0 and τ for which the cosine term in Eq. (A7) is equal to ± 1 ; i.e.,

$$B_0 - B_{\text{res}} = \frac{n\pi\hbar[1 + 2(\sigma_\omega/\omega_1)^2]}{g\mu_B} \frac{1}{\tau}, \quad n \in \mathbb{Z}. \quad (\text{A8})$$

This term represents hyperbolas in the B_0 - τ plane shown in Fig. 2.

*Current address: Lehrstuhl für Werkstoffkunde und Werkstoffmechanik, Technische Universität München, Boltzmannstraße 15, D-85748 Garching, Germany.

†Corresponding author; hoehne@wsi.tum.de

¹Y. Makhlin, G. Schön, and A. Shnirman, *Rev. Mod. Phys.* **73**, 357 (2001).

²F. Yamaguchi and Y. Yamamoto, *Appl. Phys. A* **68**, 1 (1999).

³D. Loss and D. P. DiVincenzo, *Phys. Rev. A* **57**, 120 (1998).

⁴A. Imamoglu, D. D. Awschalom, G. Burkard, D. P. DiVincenzo, D. Loss, M. Sherwin, and A. Small, *Phys. Rev. Lett.* **83**, 4204 (1999).

⁵B. E. Kane, *Nature (London)* **393**, 133 (1998).

⁶R. Vrijen, E. Yablonovitch, K. Wang, H. W. Jiang, A. Balandin, V. Roychowdhury, T. Mor, and D. DiVincenzo, *Phys. Rev. A* **62**, 012306 (2000).

⁷A. M. Tyryshkin, S. A. Lyon, A. V. Astashkin, and A. M. Raitsimring, *Phys. Rev. B* **68**, 193207 (2003).

⁸A. Morello, J. J. Pla, F. A. Zwanenburg, K. W. Chan, K. Y. Tan, H. Huebl, M. Möttönen, C. D. Nugroho, C. Yang, J. A. van Donkelaar *et al.*, *Nature (London)* **467**, 687 (2010).

⁹R. N. Ghosh and R. H. Silsbee, *Phys. Rev. B* **46**, 12508 (1992).

¹⁰C. C. Lo, J. Bokor, T. Schenkel, J. He, A. M. Tyryshkin, and S. A. Lyon, *Appl. Phys. Lett.* **91**, 242106 (2007).

¹¹G. W. Morley, D. R. McCamey, H. A. Seipel, L.-C. Brunel, J. van Tol, and C. Boehme, *Phys. Rev. Lett.* **101**, 207602 (2008).

¹²D. Kaplan, I. Solomon, and N. F. Mott, *J. Phys. (Paris)* **39**, 51 (1978).

¹³A. R. Stegner, C. Boehme, H. Huebl, M. Stutzmann, K. Lips, and M. S. Brandt, e-print [arXiv:quant-ph/0607178](https://arxiv.org/abs/quant-ph/0607178).

¹⁴F. Hoehne, H. Huebl, B. Galler, M. Stutzmann, and M. S. Brandt, *Phys. Rev. Lett.* **104**, 046402 (2010).

¹⁵D. R. McCamey, H. Huebl, M. S. Brandt, W. D. Hutchison, J. C. McCallum, R. G. Clark, and A. R. Hamilton, *Appl. Phys. Lett.* **89**, 182115 (2006).

¹⁶C. Boehme and K. Lips, *Appl. Phys. Lett.* **79**, 4363 (2001).

¹⁷C. Boehme and K. Lips, *Phys. Rev. B* **68**, 245105 (2003).

¹⁸A. R. Stegner, C. Boehme, H. Huebl, M. Stutzmann, K. Lips, and M. S. Brandt, *Nature Phys.* **2**, 835 (2006).

¹⁹H. Huebl, F. Hoehne, B. Grolik, A. R. Stegner, M. Stutzmann, and M. S. Brandt, *Phys. Rev. Lett.* **100**, 177602 (2008).

²⁰S. Y. Paik, S. Y. Lee, W. J. Baker, D. R. McCamey, and C. Boehme, *Phys. Rev. B* **81**, 075214 (2010).

²¹R. de Sousa, C. C. Lo, and J. Bokor, *Phys. Rev. B* **80**, 045320 (2009).

²²F. Boulitrop, *Phys. Rev. B* **28**, 6192 (1983).

²³A. Gliesche, C. Michel, V. Rajevac, K. Lips, S. D. Baranovskii, F. Gebhard, and C. Boehme, *Phys. Rev. B* **77**, 245206 (2008).

²⁴K. Fukui, T. Sato, H. Yokoyama, H. Ohya, and H. Kamadaz, *J. Magn. Reson.* **149**, 13 (2000).

²⁵A. Schweiger and G. Jeschke, *Principles of Pulse Electron Paramagnetic Resonance* (Oxford University Press, Oxford, 2001).

²⁶S. A. Dikanov and Y. D. Tsvetkov, *Electron Spin Echo Envelope Modulation Spectroscopy* (CRC Press, Boca Raton, 1992).

²⁷H. Blok, I. Akimoto, S. Milikisyants, P. Gast, E. Groenen, and J. Schmidt, *J. Magn. Reson.* **201**, 57 (2009).

²⁸G. Feher, *Phys. Rev.* **114**, 1219 (1959).

²⁹E. H. Poindexter, P. J. Caplan, B. E. Deal, and R. R. Razouk, *J. Appl. Phys.* **52**, 879 (1981).

³⁰A. Stesmans and V. V. Afanas'ev, *J. Appl. Phys.* **83**, 2449 (1998).

³¹A. Stesmans and V. V. Afanas'ev, *J. Phys. Condens. Matter* **10**, L19 (1998).

³²T. D. Mishima, P. M. Lenahan, and W. Weber, *Appl. Phys. Lett.* **76**, 3771 (1999).

³³C. F. Young, E. H. Poindexter, G. J. Gerardi, W. L. Warren, and D. J. Keeble, *Phys. Rev. B* **55**, 16245 (1997).

³⁴C. P. Poole, *Electron Spin Resonance* (John Wiley and Sons, New York, 1983).

³⁵E. Abe, A. Fujimoto, J. Isoya, S. Yamasaki, and K. M. Itoh, e-print [arXiv:cond-mat/0512404](https://arxiv.org/abs/cond-mat/0512404).

³⁶N. F. Ramsey, *Phys. Rev.* **78**, 695 (1950).

³⁷E. T. Jaynes, *Phys. Rev.* **98**, 1099 (1955).

³⁸A. L. Bloom, *Phys. Rev.* **98**, 1105 (1955).

³⁹R. G. DeVoe and R. G. Brewer, *Phys. Rev. Lett.* **40**, 862 (1978).

⁴⁰B. L. T. Plourde, T. L. Robertson, P. A. Reichardt, T. Hime, S. Linzen, C.-E. Wu, and J. Clarke, *Phys. Rev. B* **72**, 060506 (2005).

⁴¹A. Wallraff, D. I. Schuster, A. Blais, L. Frunzio, J. Majer, M. H. Devoret, S. M. Girvin, and R. J. Schoelkopf, *Phys. Rev. Lett.* **95**, 060501 (2005).

⁴²The factor of $\sqrt{2}$ between $\tilde{\omega}_1$ [Eq. (1)] and $\bar{\omega}_1$ [Eq. (6)] can be explained by the different excitation profiles of the corresponding pulse sequences. Since the spin-echo pulse sequence consists of two EDFID pulse sequences, the effective excitation profile of the

EDFID pulse sequence [Eq. (A4)] has to be squared to describe the spin echo. Hence, its excitation bandwidth is reduced by a factor of $\sqrt{2}$ since $[\exp(-x^2)]^2 = \exp(-[x/(1/\sqrt{2})]^2)$.

⁴³J. A. Weil and J. R. Bolton, *Electron Paramagnetic Resonance* (John Wiley and Sons, New York, 2007).

⁴⁴S. Lee, P. von Allmen, F. Oyafuso, G. Klimeck, and K. B. Whaley, *J. Appl. Phys.* **97**, 043706 (2005).

⁴⁵E. Abe, A. M. Tyryshkin, S. Tojo, J. J. L. Morton, W. M. Witzel, A. Fujimoto, J. W. Ager, E. E. Haller, J. Isoya, S. A. Lyon *et al.*, *Phys. Rev. B* **82**, 121201 (2010).